Nonvolatile Current-Modulated Four-State Magnetoplasmonic Memory

Mark E. Nowakowski[*]

Northrop Grumman Corporation, 1212 Winterson Road, Linthicum Heights, Maryland 21090, USA

The operation and readout of a nonvolatile current-modulated four-state magnetoplasmonic metal-insulator-metal (*M-I-M*) waveguide device is modeled as a function of device and material parameters. Current pulses applied to electrically isolated stacks containing a ferromagnet and an active layer (either a metal with large spin-orbit coupling or a topological insulator) embedded within a plasmonic metal (Au) situated on either side of the insulating core can switch the orientation of the magnetic layers via the spin-transfer torque mechanism. The four possible magnetic-orientation combinations interact with the surface-plasmon-polariton mode to produce four distinguishable values (on the order of 0.1–1%) of the effective index of refraction. By overcoming the optical losses traditionally associated with magnetic materials within a plasmonic environment, this four-state optical memory element is able to exploit both the robust magnetic stability of metallic magnets and the spin-torque switching mechanism that can reorient these magnets via on-chip currents without requiring external magnetic fields. Using this element, we propose a 2-stage plasmonic memory register with a range of states that can scale as 4^n for n stages.

I. INTRODUCTION

Conventional and photonic computational architectures both benefit from high-performance nonvolatile memory elements: robust and stable physical bits that can endure fast low-power switching events over many cycles. In conventional architectures, magnetic elements with stable antiparallel domains are commonly chosen; however, until recently, bulky and power-hungry external magnets were required to induce switching between the magnetic states. This limited the scalability and reduced the energy efficiency of this technology. These limitations, however, were overcome by the spintronics community with the introduction of spin-torque magnetic-random-access (ST MRAM) memories [1], which replace external-field switching with on-chip switching driven by current-induced spin-orbit torques (SOTs) [2]. SOTs are generated by spin accumulations along the surfaces of metals with large spin-orbit coupling (SOC) [3,4] or topological insulators (TIs) [5,6]. The magnetic torque generated by spin accumulations with sufficient intensity can reorient individually addressable localized magnetic domains. The reading out of spin-torque memory devices typically involves either tabletop optical setups that employ the magneto-optical Kerr effect (MOKE) [7] or setups that measure magnetic resonance or magnetoresistance [3,4]. Of these, magnetoresistance measurements, specifically magnetic tunnel junctions (MTJs), are typically chosen to

read out scalable memory devices in conventional computing architectures. Unfortunately, a corresponding readout scheme suitable for scalable photonic architectures has not yet been developed.

Surprisingly, the well-established ST MRAM community has not strongly embraced the emerging photonic-computing sector amid their efforts to develop nonvolatile photonic memories [8]. While well-known magneto-optical readout techniques are suitable for tabletop research environments, magnetic materials integrated into photonic or plasmonic circuits often introduce unacceptable losses that limit readout performance [9]. Because of this, photonics researchers have sought nonvolatile behavior in more photonically compatible alternative physical systems such as plasmonic nanoparticles [10], flash-based technologies [11], and phase-change materials [12] that are sensitive to all-optical control methods. However, none of these material systems succeed in replicating the combined stability, endurance, and low-energy switching properties possessed by ST MRAM devices. The resolution of this materials incompatibility would benefit both the photonics and the spintronics communities, producing (simultaneously) both a nonvolatile photonic memory and a device-scale depth-dependent magneto-optical sensor that may be scalable into smaller form factors than existing tabletop magneto-optical measurements [13].

The solution to this challenge requires an optimization of the presence of magnets within conventional photonic materials to maximize their measurable magnetic signals within acceptable loss margins. Initial studies [14,15] following this prescription have shown that composite

_____

[*]mark.nowakowski@ngc.com

plasmonic heterostructures, embedded with nanometers-thick magnetic layers, do not suffer severe losses. Furthermore, the off-diagonal components of the dielectric tensor in these thin magnetic layers impart a stable and measurable magneto-optical influence on the surface-plasmon-polariton (SPP) dispersion relation, which can be modeled using the effective medium approximation [16]. These proof-of-concept results, however, have employed bulky and power-hungry external magnets, limiting the scalable potential for these magnetoplasmonic devices. In this work, we propose and characterize a magnetoplasmonic device design that integrates spin-torque (ST) bilayers (magnets and materials with large SOC), introducing a nonvolatile ST MRAM memory element engineered for scalable switching within a photonic readout architecture.

First, a preliminary analysis is performed for a single heterostructure with one embedded ST layer to determine the character of the evanescent fields as a function of device, material, and magnetic variations, in order to define realistic bounds for choosing materials compatible for this demonstration. Following this, the optical transmission for a full magnetoplasmonic metal-insulator-metal (*M-I-M*) waveguide structure is analyzed, where each *M* is a metal-like heterostructure with the embedded ST layers and the insulating core *I* is SiO$_2$. We find that a device designed with unbalanced magnetic-layer thicknesses on either side of the insulating core imparts four possible index values based on the combined orientation of the two magnets. The discrete and distinguishable index values can be manipulated by independently switching either side of the device on demand via the ST mechanism, while the robust and stable magnetic layers provide the sought-after nonvolatile behavior. The anticipated switching currents, rates, and scalability of such a device are briefly discussed and, finally, a proposal for a nonvolatile plasmonic memory waveguide register employing *n* magnetplasmonic elements is considered, which imparts a range of states that can scale as 4^n.

II. ANALYSIS OF A SINGLE-SIDED INTERFEROMETER HETEROSTRUCTURE

A cross section for the proposed heterostructure is shown in Figs. 1(c) and 1(d). It is a bilayer stack composed of a thin magnet (thickness *c*, dielectric constant ϵ_{mag}) directly adjacent to a metal with large SOC or a TI (*d*, ϵ_{sh}), encased between two thin dielectric layers that provide electrical isolation (*b*, ϵ_{iso}) and surrounded on either side by a metal optimized for plasmon propagation (ϵ_m), where the top layer has a thickness *a* and the bottom layer is assumed to be large compared to the other layer thicknesses. The magnetoplasmonic influence of the SPP dispersion for this stack can be measured using a plasmonic interferometer, as shown in Appendix A. The well-documented analysis from such experiments extracts
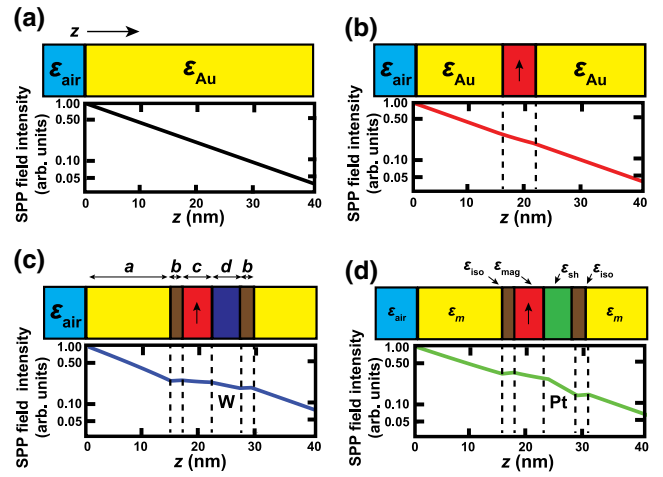

FIG. 1. Cross sections and SPP field intensities at $\lambda = 808$ nm for four plasmonic stacks: (a) air/Au, (b) air/Au(15)/Co(6)/Au, (c) air/Au(15)/MgO(2)/CoFeB(5)/W(5)/MgO(2)/Au, and (d) air/Au(15)/MgO(2)/CoFeB(5)/Pt(5)/MgO(2)/Au. In part (c), the layer thicknesses (*a*, *b*, *c*, and *d*) are indicated. In part (d), the generic dielectric constants (ϵ_m, ϵ_{iso}, ϵ_{mag}, and ϵ_{sh}) are indicated.

a figure of merit known as the magnetoplasmonic sensitivity: $|\Delta k_{\mathrm{mp}}|L_{\mathrm{SPP}}$, where $|\Delta k_{\mathrm{mp}}|$ is the SPP wave-vector difference between antiparallel magnetic orientations and L_{SPP} is the SPP propagation length [14,15]. For this analysis, the dielectric constants in each layer have been chosen assuming a wavelength $\lambda = 808$ nm; however, studies have indicated that SPP modulation is possible over a broad range of wavelengths [14,15,17].

The model for this heterostructure examines the magnetoplasmonic influence of bilayer stacks composed of a 5-nm CoFeB magnet and a 5-nm-thick layer of either W or Pt, encased within two 2-nm MgO dielectric layers [see Figs. 1(c) and 1(d), respectively]. This choice is motivated by the geometries of experimentally verified devices that have demonstrated ST-based switching [3,4,6]. In these materials, the current-induced spin Hall effect generates an interfacial surface-spin accumulation that drives the ST mechanism; therefore, for brevity, we generally call this electrically active layer the spin Hall layer. Alternatively, a topological insulator, such as Bi$_2$Se$_3$, which generates similar surface-spin accumulations via spin-momentum locking [5,6], could replace these spin Hall metals; however, that case is not considered.

The magnetic-orientation-dependent plasmonic signal level $|\Delta k_{\mathrm{mp}}| = |k_x^{M=1} - k_x^{M=-1}|$ and SPP propagation length, $L_{\mathrm{SPP}}^{M=\pm 1}$, are estimated by solving for the dispersion relation of this system, where $M = \pm 1$ indicates the antiparallel magnetic orientations and $k_x^{M=\pm 1}$ are the heterostructure propagation constants for each case. Solutions are obtained numerically by solving a system of equations consisting of the wave equation in each material layer and

the determinant of a matrix formed from enforcing boundary conditions at each interface, as shown in Appendix B [18]. Notably, the dielectric tensor of the magnetic layer possesses off-diagonal elements, ϵ_{xz}, which are limited to first order. The parity of ϵ_{xz} is magnetic-orientation dependent and influences the electric-field component of the SPP modes in the model, giving rise to the magnetoplasmonic signal $|\Delta k_{mp}|$.

Figures 1(a)–1(d) plot the SPP field profile as a function of depth for four structures: a standard air/Au interface (black), an air/Au(15 nm)/Co(6)/Au geometry measured in a previous study [14] (red), and the proposed geometries, air/Au(15)/MgO(2)/CoFeB(5)/XX(5)/MgO(2)/Au, where XX is either W (blue) or Pt (green), respectively. These curves are generated assuming complex optical dielectric constants obtained from the literature at $\lambda = 808$ nm for each material: $\epsilon_{Au} = -24.80 + 1.50i$, $\epsilon_{Co} = -17.10 + 24.20i$, $\epsilon_{CoFeB} = -0.33 + 21.45i$, $\epsilon_{Pt} = -66.40 + 9.52i$, $\epsilon_W = -12.8 + 8.01i$, and $\epsilon_{MgO} = 2.98$. In the model, the influence of the magnetic layer is $q = i\epsilon_{xz}/\epsilon_{mag}$, where ϵ_{mag} is either ϵ_{Co} or ϵ_{CoFeB}, respectively. For both Co and CoFeB, we assume the value of $q = 0.0345 + 0.0100i$ [14]. These data indicate that the presence of W, Pt, and the MgO layers does not contribute to a significant deviation of the field profile compared to the air/Au interface, in a manner similar to the Au/Co/Au stack. In fact, the dielectric layers enhance the field strength. From these plots, we conclude that the small perturbations to the SPP environment introduced by the W, Pt, and MgO thin films do not prohibit the proposed device functionality.

The potential effectiveness of the proposed device is explored in Fig. 2(a), which compares the magnetoplasmonic sensitivity of the Au/Co/Au stack (red) to the proposed stack with either a 5-nm Pt (green) or W (blue) layer as a function of the capping Au thickness a. As a increases, the active bilayer is pushed farther from

the surface, reducing its sensitivity. Previous studies [14] have measured magnetic signals from embedded layers approximately 50 nm deep into the surface—this point is indicated on Fig. 2(a) and its sensitivity value is approximately 0.0015. We consider this value the minimum signal threshold required to detect an analogous current-induced magnetic reorientation. According to the model, the sensitivities of both proposed devices meet this criterion for thicknesses $a < 50$ nm for both W and Pt. Even though the maximal values in all three proposed devices are less than the Au/Co/Au stack, we expect, based on previous experimental results, that a current-induced magnetic reorientation will be observable using the interferometer geometry. Moreover, this plot also highlights the value of this design as a depth-sensitive device-scale magneto-optical sensor that complements existing tabletop MOKE setups. In contrast to the depth profile of Gaussian beams that laterally change based on the spot size [13], the evanescent light profile in the magnetoplasmonic device is laterally uniform to the extent of the device geometry. This ensures that a global signal is measured over the entire magnetic thin film or interface under test, simplifying data interpretation. Furthermore, employing a photonic readout with this geometry permits a more scalable magneto-optical sensor form factor, in contrast to conventional tabletop probes.

The spin Hall layer could be replaced with another material, such as a TI [5,6]; however, the complex optical dielectric constants for such thin-film replacements may not be known. The complex optical dielectric parameter space for the stack—Au(15)/MgO(2)/CoFeB(5)/XX(5)/MgO(2)/Au, where XX is the replacement spin Hall layer—is explored in Fig. 2(b). The influence on the magnetoplasmonic sensitivity of the replacement layer XX is studied by varying the real and imaginary optical constants in the ranges -70–0 and 0–30, respectively. We indicate the values that we used for Pt and W in Fig. 2(a) on this
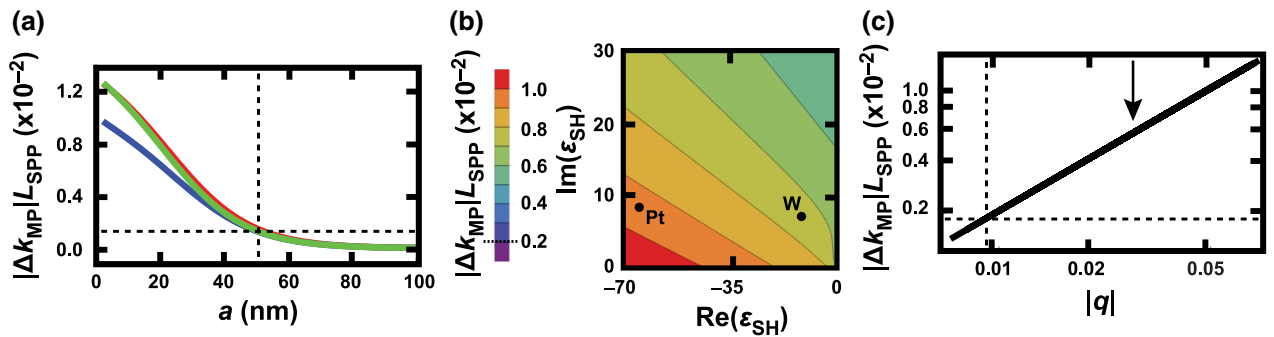

FIG. 2. (a) $|\Delta k_{mp}|L_{SPP}$ vs the capping Au thickness for Au(a)/Co(6)/Au (red) and Au(a)/MgO(2)/CoFeB(5)/XX(5)/MgO(2)/Au, for XX = W (blue) and Pt (green). The horizontal dashed line indicates the upper bound of the experimentally detected limit, while the vertical dashed line is a guide to the eye [14]. (b) $|\Delta k_{mp}|L_{SPP}$ vs Re(ϵ_{sh}) and Im(ϵ_{sh}) for Au(15)/MgO(2)/CoFeB(5)/XX(5)/MgO(2)/Au. Values for ϵ_{Pt} and ϵ_W are indicated. The dashed line in the color scale indicates the detection limit identified in part (a). (c) $|\Delta k_{mp}|L_{SPP}$ vs $|q|$ for Au(15)/MgO(2)/CoFeB(5)/W(5)/MgO(2)/Au. The horizontal dashed line indicates the detection limit identified in part (a) while the vertical dashed line is a guide to the eye. The value of $|q|$ used in parts (a) and (b) is indicated with an arrow.

plot. Using the same sensitivity threshold as before (indicated by the dashed line on the color scale), this plot finds that, for the assumed thicknesses, a substitute material with large SOC possessing a complex optical dielectric value anywhere within the plotted range of reasonable values would still permit an acceptable magnetoplasmonic signal.

Until now, we have assumed a fixed contribution from the off-diagonal magnetic dielectric term q; however, the magnitude of this value is also material dependent. In Fig. 2(c), we plot the magnetoplasmonic sensitivity for a range of $|q|$, as the real and imaginary components of q are varied from 0 to 0.05, for the stack Au(15)/MgO(2)/CoFeB(5)/W(5)/MgO(2)/Au, and indicate the value we have used in our previous plots with an arrow. Because ϵ_{xz} is taken to first order, we observe a linear dependence between the magnetoplasmonic sensitivity and $|q|$. It is important to consider this relationship in the context of choosing a ferromagnet as a nonvolatile memorylike element within a magnetoplasmonic device. While the strength of $|q|$ may vary between ferromagnets, these results indicate that reasonable sensitivities ($|\Delta k_{mp}|L_{SPP} > 0.0015$) may be obtained for values of $|q| > 0.01$; this is approximately 3 times lower than the value we had previously assumed, and suggests that a wide variety of magnets could be selected as the active memory component for this device.

III. ANALYSIS OF A DOUBLE-SIDED WAVEGUIDE HETEROSTRUCTURE

Encouraged by these results, we now examine the optical transmission dependence of a *M-I-M*-like plasmonic waveguide, where the M for either side consists of the previously modeled plasmonic stack with the embedded ST layers and the insulating core I has a thickness e and a dielectric constant ϵ_{core}. A cross section of the proposed device is shown in Fig. 3(a). The bilayer stacks on either side of the insulating core are mirrored to achieve symmetric magnetic influences. Additionally, fabrication by evaporation or sputtering permits the magnetic-layer thickness on either side to be independently tuned with high precision (< 1 nm). The magnetic-layer thicknesses for sides 1 and 2 are c_1 and c_2, respectively; otherwise, the remaining thickness values and dielectric constants are identical to those of the previous model. Since this waveguide geometry replaces the interferometer geometry, analyzing this system by extracting $|\Delta k_{mp}|L_{SPP}$ is no longer appropriate. Instead, the *M-I-M* heterostructure is characterized by the effective index of refraction $n_{eff} = \text{Re}(k_x/k_0)$, where k_x, in this case, is the propagation constant numerically calculated for each possible magnetic-orientation combination and $k_0 = 2\pi/\lambda$, as shown in Appendix C. For this model, the same materials are chosen as before; however, this time only W is chosen for the spin Hall layers, due to its larger value of the spin Hall angle [4]. Finally, SiO$_2$
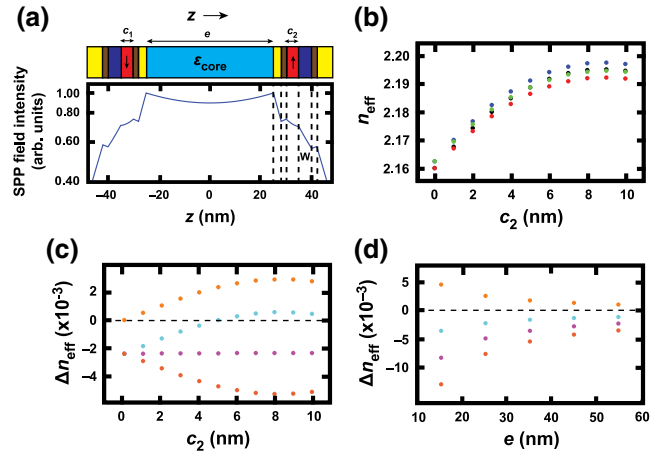

FIG. 3. (a) The cross section and SPP field intensities at $\lambda = 808$ nm for the *M-I-M*-like plasmonic waveguide stack Au/MgO(2)/W(5)/CoFeB(5)/MgO(2)/Au(3)/SiO$_2$(50)/ Au(3)/MgO(2)/CoFeB(5)/W(5)/MgO(2)/Au. (b) The effective index of refraction of the device, n_{eff}, as a function of c_2 (at $c_1 = 5$ nm) for each magnetic combination: UU (black), UD (red), DU (blue), and DD (green). (c) The optical distinguishability Δn_{eff} as a function of c_2 for the magnetic-state combinations UU-UD (orange), UU-DU (magenta), UU-DD (cyan), and UD-DU (tan). A dashed line at zero indicates where states are optically indistinguishable. (d) The optical distinguishability Δn_{eff} for each state combination as a function of the core thickness e for $c_1 = 5$ nm and $c_2 = 2.5$ nm.

($\epsilon_{SiO_2} = 2.11$) is selected as the core material to minimize losses [19].

Assuming the values $c_1 = 5$ nm and $e = 50$ nm, Fig. 3(b) plots n_{eff} as a function of the c_2 thickness from 0 to 10 nm at 1 nm intervals for each possible orientation combination: up-up (UU, black), up-down (UD, red), down-up (DU, blue), and down-down (DD, green) for sides 1 and 2, respectively. The q for the c_2 layer is linearly scaled with respect to the c_2 thickness. The optical distinguishability for each state combination at each c_2 thickness is emphasized in Fig. 3(c), where the effective index differences Δn_{eff} are calculated for the UU-UD (orange), UU-DU (magenta), UU-DD (cyan), and UD-DU (tan) combinations. The DD-DU and DD-UD differences are identical to UU-UD and UU-DU by symmetry. Importantly, for a device with a magnet on only one side of the core ($c_2 = 0$), the opposing magnetic orientations produce two distinct index levels, which correspond to two distinguishable optical transmission values. This result, on its own, confirms that magnetic states fabricated with ST-like switching controls can impart nonvolatile behavior onto the effective refractive index, which can, in principle, be read out by a photonic or, in this case, a plasmonic circuit. This device-scale magneto-optical readout is the photonic circuit dual to a conventional MTJ magnetoresistance readout. Furthermore, this design only dissipates power

during switching, in contrast to conventional MTJ-based ST MRAM devices that require modest magnetoresistive sensing currents in addition to switching-current pulses.

In devices with ST layers on both sides of the core ($c_2 > 0$) that are nonsymmetric ($c_1 \neq c_2$), four distinct optically distinguishable states emerge, shown in Figs. 3(b) and 3(c), corresponding to the difference between the magnetic states on either side of the core. When $c_1 = c_2$, the UU and DD states become indistinguishable. Maximizing the magneto-optical distinguishability requires balancing the trade-off between the UU-UD and UU-DD states; as c_2 approaches c_1, UU-DD diminishes while UU-UD grows, as indicated by the orange and cyan data points in Fig. 3(c). A suitable balance arises near $c_2 = c_1/2$. In Fig. 3(d), the four state distinguishabilities are plotted as a function of the core thickness e, which is varied between 15 and 55 nm at 10 nm intervals for $c_1 = 5$ nm and $c_2 = 2.5$ nm. Unsurprisingly, as e decreases, the fields from both M sides of the waveguide interact more strongly, leading to a strong core-thickness dependence of the optical distinguishability, which can reach values of order 10^{-3}–10^{-2} or 0.1–1% of n_{eff}. The maximization of the signal-to-noise ratio in a fabricated device will depend strongly on this parameter.

Scaling of the waveguide length can further minimize plasmonic losses. The embedded ST structures are robust to scaling in this dimension. Similar ST stacks fabricated to submicron lateral length scales possessing similar thicknesses to the optimized M-I-M device have switched with critical currents on the order of 100s of μA [3,4]. Equations regarding the scalability of critical currents in these geometries are well known [3,4,20,21] and are anticipated to also apply to the M-I-M waveguide device. Furthermore, current-based magnetic switching techniques have been shown to operate with subnanosecond pulses, suggesting the potential for operating these magnetoplasmonic waveguides in the gigahertz regime [22,23].

IV. A PROPOSAL FOR A MAGNETOPLASMONIC NONVOLATILE MEMORY REGISTER

When combined with the proven stability and endurance offered by the magnets, these scaling and switching metrics reveal a previously unexploited, yet realistic, device pathway to achieve nonvolatile memory within a photonic device. Consider the plasmonic waveguide in Fig. 4(a), with two magnetoplasmonic element stages spaced by Δ (where Δ can be on the order of 100s of nm or less [3,4]). The effective index of refraction within the waveguide adjacent to these magnetic elements is $n_{mag}^{1,2}$, compared to a nominal value n_{nom}. Assuming no transmission loss, light channeled through the waveguide will experience four index-of-refraction boundaries (two for each stage) that will impart some reflection that will depend on the
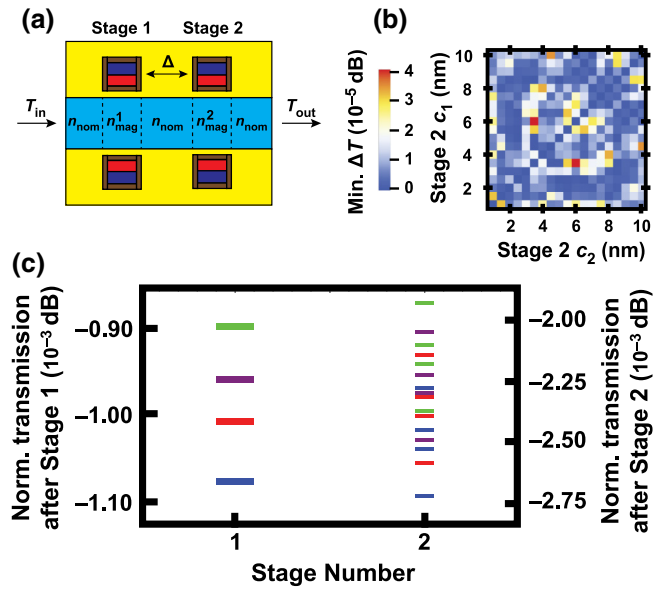

FIG. 4. (a) A schematic of a 2-stage plasmonic memory register that employs the ST-based memory element. Each memory element is spaced by Δ and generates a spatially isolated effective index of refraction $n_{mag}^{1,2}$ relative to the nominal index of refraction within the waveguide n_{nom}. (b) The minimum transmission distinguishability after stage 2 for all magnetic permutations as a function of the stage 2 c_1 and c_2 values. (c) The expected transmission after each stage, assuming no loss, for all magnetic permutations for $c_1 = 5$ nm and $c_2 = 2.5$ nm in stage 1 and $c_1 = 6$ nm and $c_2 = 3.5$ nm in stage 2. The colors indicate transmission originating from the stage 1 magnetic orientation: red (UU), blue (UD), green (DU), and purple (DD).

relative magnetic orientations in each stage, as shown in Appendix D.

For stage 1 with $c_1 = 5$ nm and $c_2 = 2.5$ nm, the expected normalized transmission for UU (red), UD (blue), DU (green), and DD (purple) is shown in Fig. 4(c). The transmitted light then encounters two more magnetically dependent barriers at stage 2. For suitably chosen stage 2 c_1 and c_2 values, 16 distinct transmission values are permitted, based on the magnetic permutations from both stages. The systematic minimum-transmission distinguishability between any two individual levels after the second stage (ΔT) is plotted in Fig. 4(b) as the values for the stage 2 c_1 and c_2 thicknesses are varied from 1 to 10 nm in steps of 0.5 nm. The maximum value of this plot is found for stage 2 c_1 and c_2 thicknesses of 6 and 3.5 nm, respectively; however, additional step resolution may suggest other levels with even more separation. The transmission response after stage 2 for these values, plotted in Fig. 4(c), reveals 16 distinct transmission levels. Further stages would continue this trend, leading to a maximum number of states that scales as 4^n for n stages. Distinguishing all of these values, however, will ultimately depend on the resolution limit of

the readout equipment. This unprecedented 4^n scaling factor exceeds the 2^n scaling of conventional ST MRAM and is a direct consequence of having ST layers on both sides of the waveguide.

V. CONCLUSION

The operational principle of this memory device fuses the well-established cornerstone traits of the ST MRAM and photonics research communities. The potential applications of this device design, though, extend well beyond a nonvolatile photonic memory. Many active spintronic research efforts rely on tabletop setups to demonstrate all-optical proof-of-concept experiments in a wide variety of material systems, including III–V semiconductors and defect centers in diamond or SiC. The integration of these materials within photonic circuits such as the one proposed here could further advance existing efforts [24] to technologically exploit exciting emergent spintronic physics in a more scalable manner. Collaborative efforts from orthogonal research fields, such as the one suggested in this work, may inspire other photonic device concepts that can probe new physics or enable new technological opportunities.

ACKNOWLEDGMENTS

APPENDIX A: INTERFEROMETER MEASUREMENT GEOMETRY

To create a plasmonic interferometer similar to the one demonstrated by Temnov *et al.* [14], focused-ion-beam (FIB) cuts are required to create a transparent through slit and a slanted groove consisting of only the capping metal in the stack, as shown in Fig. 5. The slit is oriented along the y axis (parallel to the magnetization direction) and the groove is at an angle θ with respect to the y axis. In this geometry, plasmonic light, excited by a laser source with wavelength λ, propagates along the surface and interferes with the light transmitted through the slit.

APPENDIX B: EXTRACTING PROPAGATION CONSTANTS FROM THE INTERFEROMETER GEOMETRY

A laser of wavelength λ excites surface plasmon polaritons (SPPs) at the surface of a heterostructure stack; the layers of this stack are explicitly defined in Table I. The magnetic-field components of the resulting SPP in each
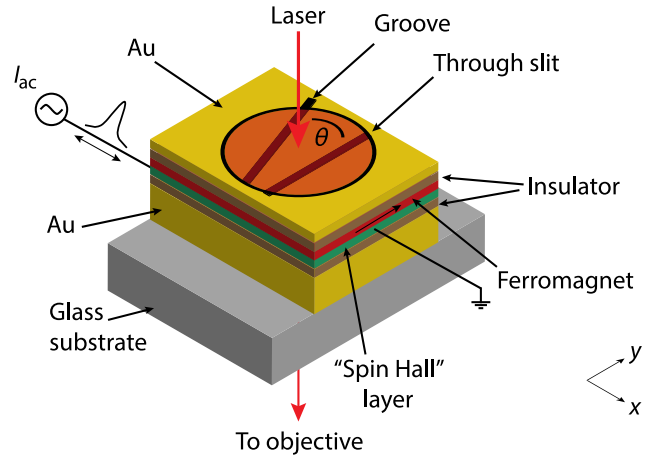

FIG. 5. An experimental schematic of the plasmonic interferometer geometry.

layer are assumed to have the following form:

$$H_{y1} = Ae^{-k_{\text{air}}z}e^{i(k_x x - \omega t)},$$

$$H_{y2} = [Be^{k_m z} + Ce^{-k_m(z+a)}]e^{i(k_x x - \omega t)},$$

$$H_{y3} = [De^{k_{\text{iso}}(z+a)} + Ee^{-k_{\text{iso}}(z+a+b)}]e^{i(k_x x - \omega t)},$$

$$H_{y4} = [Fe^{k_{\text{mag}}(z+a+b)} + Ge^{-k_{\text{mag}}(z+a+b+c)}]e^{i(k_x x - \omega t)},$$

$$H_{y5} = [He^{k_{\text{sh}}(z+a+b+c)} + Ie^{-k_{\text{sh}}(z+a+b+c+d)}]e^{i(k_x x - \omega t)},$$

$$H_{y6} = [Je^{k_{\text{iso}}(z+a+b+c+d)} + Ke^{-k_{\text{sh}}(z+a+2b+c+d)}]e^{i(k_x x - \omega t)},$$

$$H_{y7} = Le^{k_m(z+a+2b+c+d)}e^{i(k_x x - \omega t)}.$$

Maxwell equations are used to derive the SPP electric-field components:

$$-\partial_z H_y = \frac{\partial D_x}{\partial t},$$

$$\partial_x H_y = \frac{\partial D_z}{\partial t},$$

where $\overrightarrow{D} = \epsilon \overrightarrow{E}$ is the displacement field and

$$\epsilon = \begin{pmatrix} \epsilon_{xx} & 0 & 0 \\ 0 & \epsilon_{xx} & 0 \\ 0 & 0 & \epsilon_{xx} \end{pmatrix}$$

is the dielectric tensor for nonmagnetic layers, while

$$\epsilon = \begin{pmatrix} \epsilon_{xx} & 0 & \pm\epsilon_{xz} \\ 0 & \epsilon_{xx} & 0 \\ \mp\epsilon_{xz} & 0 & \epsilon_{xx} \end{pmatrix}$$

is the dielectric tensor for the magnetic layers; ϵ_{xx} is the bulk dielectric value for any individual layer (i.e.,

TABLE I. The interferometer geometry boundary conditions.

Layer number	Layer medium	Dielectric constant	Layer boundaries
1	Air	ϵ_{air}	$z > 0$
2	Plasmonic metal	ϵ_m	$0 > z > -a$
3	Isolating dielectric	ϵ_{iso}	$-a > z > -(a+b)$
4	Magnet	ϵ_{mag}	$-(a+b) > z > -(a+b+c)$
5	Spin Hall or TI	ϵ_{sh}	$-(a+b+c) > z > -(a+b+c+d)$
6	Isolating dielectric	ϵ_{iso}	$-(a+b+c+d) > z > -(a+2b+c+d)$
7	Plasmonic metal	ϵ_m	$z < -(a+2b+c+d)$

$\epsilon_m, \epsilon_{\text{iso}}, \epsilon_{\text{mag}}$, etc.), and ϵ_{xz} is the off-diagonal component generated from the magnetic polarization ($M = \pm 1$). Calculating $\vec{D}$ generally for each layer gives

$$
\begin{pmatrix} \epsilon_{xx} & 0 & \pm\epsilon_{xz} \\ 0 & \epsilon_{xx} & 0 \\ \mp\epsilon_{xz} & 0 & \epsilon_{xx} \end{pmatrix} \begin{pmatrix} E_x \\ E_y \\ E_z \end{pmatrix} = \begin{pmatrix} \epsilon_{xx}E_x \pm \epsilon_{xz}E_z \\ 0 \\ \epsilon_{xx}E_z \mp \epsilon_{xz}E_x \end{pmatrix},
$$

where $\epsilon_{xz} \to 0$ for nonmagnetic layers. Plugging $\vec{D}$ into the Maxwell equations gives

$$
-\partial_z H_y = \frac{\partial D_x}{\partial t} = \frac{\partial}{\partial t}(\epsilon_{xx}E_x \pm \epsilon_{xz}E_z),
$$

$$
\partial_x H_y = \frac{\partial D_z}{\partial t} = \frac{\partial}{\partial t}(\epsilon_{xx}E_z \mp \epsilon_{xz}E_x).
$$

Solving this system of equations for E_x gives

$$
\frac{\partial}{\partial t}E_x = \frac{\mp(\epsilon_{xz}/\epsilon_{xx})\partial_x H_y - \partial_z H_y}{(\epsilon_{xx} + \epsilon_{xz}^2/\epsilon_{xx})}.
$$

Assuming that E_x has a form similar to H_y, the SPP electric-field components in each region, n, are given by

$$
\frac{\partial}{\partial t}E_x = -i\omega E_x,
$$

$$
E_{x,n} = \frac{\mp(\epsilon_{xz,n}/\epsilon_{xx,n})\partial_x H_{y,n} - \partial_z H_{y,n}}{-i\omega(\epsilon_{xx,n} + \epsilon_{xz,n}^2/\epsilon_{xx,n})}.
$$

Taking ϵ_{xz} to first order ($\epsilon_{xz}^2 \to 0$) gives

$$
E_{x,n} = \frac{\mp(\epsilon_{xz,n}/\epsilon_{xx,n})\partial_x H_{y,n} - \partial_z H_{y,n}}{-i\omega\epsilon_{xx,n}}.
$$

Next, the following boundary conditions are applied at each interface:

$$
H_n = H_{n+1},
$$

$$
E_n = E_{n+1}.
$$

After setting $i\epsilon_{xz}/\epsilon_{\text{mag}} \to q$, the resulting boundary condition equations form a system of equations $A_{\text{mat}}X = 0$, where A_{mat} is as follows:

$$
\begin{pmatrix}
1 & -1 & -e^{-k_m a} & 0 & 0 & 0 & 0 & 0 & 0 & 0 & 0 & 0 \\
\frac{k_{\text{air}}}{\epsilon_{\text{air}}} & \frac{k_m}{\epsilon_m} & -\frac{k_m}{\epsilon_m}e^{-k_m a} & 0 & 0 & 0 & 0 & 0 & 0 & 0 & 0 & 0 \\
0 & e^{-k_m a} & 1 & -1 & -e^{-k_{\text{iso}} b} & 0 & 0 & 0 & 0 & 0 & 0 & 0 \\
0 & \frac{k_m}{\epsilon_m}e^{-k_m a} & -\frac{k_m}{\epsilon_m} & -\frac{k_{\text{iso}}}{\epsilon_{\text{iso}}} & \frac{k_{\text{iso}}}{\epsilon_{\text{iso}}}e^{-k_{\text{iso}} b} & 0 & 0 & 0 & 0 & 0 & 0 & 0 \\
0 & 0 & 0 & e^{-k_{\text{iso}} b} & 1 & -1 & -e^{-k_{\text{mag}} c} & 0 & 0 & 0 & 0 & 0 \\
0 & 0 & 0 & \frac{k_{\text{iso}}}{\epsilon_{\text{iso}}}e^{-k_{\text{iso}} b} & -\frac{k_{\text{iso}}}{\epsilon_{\text{iso}}} & -\frac{(k_{\text{mag}} \pm qk_x)}{\epsilon_{\text{mag}}} & \frac{(k_{\text{mag}} \mp qk_x)}{\epsilon_{\text{mag}}}e^{-k_{\text{mag}} c} & 0 & 0 & 0 & 0 & 0 \\
0 & 0 & 0 & 0 & 0 & e^{-k_{\text{mag}} c} & 1 & -1 & -e^{-k_{\text{sh}} d} & 0 & 0 & 0 \\
0 & 0 & 0 & 0 & 0 & \frac{(k_{\text{mag}} \pm qk_x)}{\epsilon_{\text{mag}}}e^{-k_{\text{mag}} c} & -\frac{(k_{\text{mag}} \mp qk_x)}{\epsilon_{\text{mag}}} & -\frac{k_{\text{sh}}}{\epsilon_{\text{sh}}} & \frac{k_{\text{sh}}}{\epsilon_{\text{sh}}}e^{-k_{\text{sh}} d} & 0 & 0 & 0 \\
0 & 0 & 0 & 0 & 0 & 0 & 0 & e^{-k_{\text{sh}} d} & 1 & -1 & -e^{-k_{\text{iso}} b} & 0 \\
0 & 0 & 0 & 0 & 0 & 0 & 0 & \frac{k_{\text{sh}}}{\epsilon_{\text{sh}}}e^{-k_{\text{sh}} d} & -\frac{k_{\text{sh}}}{\epsilon_{\text{sh}}} & -\frac{k_{\text{iso}}}{\epsilon_{\text{iso}}} & \frac{k_{\text{iso}}}{\epsilon_{\text{iso}}}e^{-k_{\text{iso}} b} & 0 \\
0 & 0 & 0 & 0 & 0 & 0 & 0 & 0 & 0 & e^{-k_{\text{iso}} b} & 1 & -1 \\
0 & 0 & 0 & 0 & 0 & 0 & 0 & 0 & 0 & \frac{k_{\text{iso}}}{\epsilon_{\text{iso}}}e^{-k_{\text{iso}} b} & -\frac{k_{\text{iso}}}{\epsilon_{\text{iso}}} & -\frac{k_m}{\epsilon_m}
\end{pmatrix}
$$

.

TABLE II.   Waveguide geometry boundary conditions.

Layer number	Layer medium	Dielectric constant	Layer boundaries
1	Plasmonic metal	ϵ_m	$z > (a + 2b + c_1 + d + \frac{e}{2})$
2	Isolating dielectric	ϵ_{iso}	$(a + 2b + c_1 + d + \frac{e}{2} > z > (a + b + c_1 + d + \frac{e}{2})$
3	Spin Hall or TI	ϵ_{sh}	$(a + b + c_1 + d + \frac{e}{2} > z > (a + b + c_1 + \frac{e}{2})$
4	Magnet	ϵ_{mag}	$(a + b + c_1 + \frac{e}{2}) > z > (a + b + \frac{e}{2})$
5	Isolating dielectric	ϵ_{iso}	$(a + b + \frac{e}{2}) > z > (a + \frac{e}{2})$
6	Plasmonic metal	ϵ_m	$(a + \frac{e}{2}) > z > \frac{e}{2}$
7	Insulating core	ϵ_{core}	$\frac{e}{2} > z > -\frac{e}{2}$
8	Plasmonic metal	ϵ_m	$-\frac{e}{2} > z > -(a + \frac{e}{2})$
9	Isolating dielectric	ϵ_{iso}	$-(a + \frac{e}{2}) > z > -(a + b + \frac{e}{2})$
10	Magnet	ϵ_{mag}	$-(a + b + \frac{e}{2}) > z > -(a + b + c_2 + \frac{e}{2})$
11	Spin Hall or TI	ϵ_{sh}	$-(a + b + c_2 + \frac{e}{2}) > z > -(a + b + c_2 + d + \frac{e}{2})$
12	Isolating dielectric	ϵ_{iso}	$-(a + b + c_2 + d + \frac{e}{2}) > z > -(a + 2b + c_2 + d + \frac{e}{2})$
13	Plasmonic metal	ϵ_m	$z < -(a + 2b + c_2 + d + \frac{e}{2})$

To extract the propagation constants, the following system of equations must be solved; these enforce the boundary conditions and account for the wave equation in each heterostructure layer. Note that ϵ_{xz} is again taken to first order:

$$k_x^2 = k_{\mathrm{air}}^2 + \epsilon_{\mathrm{air}} k_0^2,$$
$$k_x^2 = k_m^2 + \epsilon_m k_0^2,$$
$$k_x^2 = k_{\mathrm{iso}}^2 + \epsilon_{\mathrm{iso}} k_0^2,$$
$$k_x^2 = k_{\mathrm{mag}}^2 + \epsilon_{\mathrm{mag}} k_0^2,$$
$$k_x^2 = k_{\mathrm{sh}}^2 + \epsilon_{\mathrm{sh}} k_0^2,$$
$$\det A_{\mathrm{mat}} = 0,$$

where k_x is the heterostructure propagation constant, k_{air}, k_m, k_{iso}, k_{mag}, and k_{sh} are the perpendicular wave-vector components in each region, and $k_0 = \omega/c = 2\pi/\lambda$. This system is then solved numerically. The magnetoplasmonic signal, $|\Delta k_{\mathrm{mp}}| L_{\mathrm{SPP}}$, is obtained after solving this system for both magnetic polarization conditions ($M = \pm 1$), where

$$|\Delta k_{\mathrm{mp}}| = |k_x^{M=1} - k_x^{M=-1}|$$
$$L_{\mathrm{SPP}} = \frac{1}{2 \mathrm{Im}(k_x)}.$$

APPENDIX C: EXTRACTING PROPAGATION CONSTANTS FROM WAVEGUIDE GEOMETRY

A laser of wavelength λ excites surface-plasmon-polariton (SPP) modes in an *M-I-M*-like plasmonic waveguide structure; the layers of this stack are explicitly defined in Table II. The magnetic-field components of the resulting SPP in each layer are assumed to have the following form:

$$H_{y1} = Ae^{-k_m(z - (a+b+c_1+d+e/2))} e^{i(k_x x - \omega t)},$$
$$H_{y2} = [Be^{k_{\mathrm{iso}}(z - (a+b+c_1+e/2))} + Ce^{-k_{\mathrm{iso}}(z - (a+b+c_1+e/2))}]$$

$$e^{i(k_x x - \omega t)},$$
$$H_{y3} = [De^{k_{\mathrm{sh}}(z - (a+b+e/2))} + Ee^{-k_{\mathrm{sh}}(z - (a+b+e/2))}] e^{i(k_x x - \omega t)},$$
$$H_{y4} = [Fe^{k_{\mathrm{mag}}(z - (a+e/2))} + Ge^{-k_{\mathrm{mag}}(z - (a+e/2))}] e^{i(k_x x - \omega t)},$$
$$H_{y5} = [He^{k_{\mathrm{iso}}(z - e/2)} + Ie^{-k_{\mathrm{iso}}(z - e/2)}] e^{i(k_x x - \omega t)},$$
$$H_{y6} = [Je^{k_m z} + Ke^{-k_m z}] e^{i(k_x x - \omega t)},$$
$$H_{y7} = [Le^{k_{\mathrm{core}} z} + Me^{-k_{\mathrm{core}} z}] e^{i(k_x x - \omega t)},$$
$$H_{y8} = [Ne^{k_m z} + Oe^{-k_m z}] e^{i(k_x x - \omega t)},$$
$$H_{y9} = [Pe^{k_{\mathrm{iso}}(z + e/2)} + Qe^{-k_{\mathrm{iso}}(z + e/2)}] e^{i(k_x x - \omega t)},$$
$$H_{y10} = [Re^{k_{\mathrm{mag}}(z + a + e/2)} + Se^{-k_{\mathrm{mag}}(z + a + e/2)}] e^{i(k_x x - \omega t)},$$
$$H_{y11} = [Te^{k_{\mathrm{sh}}(z + a + b + e/2)} + Ue^{-k_{\mathrm{sh}}(z + a + b + e/2)}] e^{i(k_x x - \omega t)},$$
$$H_{y12} = [Ve^{k_{\mathrm{iso}}(z + a + b + c_2 + e/2)} + We^{-k_{\mathrm{iso}}(z + a + b + c_2 + e/2)}]$$

$$e^{i(k_x x - \omega t)},$$
$$H_{y13} = Xe^{k_m(z + a + b + c_2 + d + e/2)} e^{i(k_x x - \omega t)},$$

The SPP electric-field components in each region are calculated in a manner identical to those for the interferometer device. Taking ϵ_{xz} to first order gives

$$E_{x,n} = \frac{\mp (\epsilon_{xz,n}/\epsilon_{xx,n}) \partial_x H_{y,n} - \partial_z H_{y,n}}{-i\omega \epsilon_{xx,n}}.$$

Applying boundary conditions at each interface and taking $i\epsilon_{xz}/\epsilon_{\mathrm{mag}} \to q$ gives a system of boundary-condition equations, A_{mat}, similar to those for the interferometer device. To extract the propagation constant for each magnetic-orientation combination, the following system of equations is solved, which enforces the boundary conditions and accounts for the wave equation in each heterostructure

layer. Note that ϵ_{xz} is still taken to first order:

$$k_x^2 = k_m^2 + \epsilon_m k_0^2,$$
$$k_x^2 = k_{\text{iso}}^2 + \epsilon_{\text{iso}} k_0^2,$$
$$k_x^2 = k_{\text{mag}}^2 + \epsilon_{\text{mag}} k_0^2,$$
$$k_x^2 = k_{\text{sh}}^2 + \epsilon_{\text{sh}} k_0^2,$$
$$k_x^2 = k_{\text{core}}^2 + \epsilon_{\text{core}} k_0^2,$$
$$\det A_{\text{mat}} = 0.$$

Four separate k_x solutions are obtained for each magnetization combination, where the directions correspond to the orientation on side 1 and 2 of the core, respectively: up-up (UU), up-down (UD), down-up (DU), and down-down (DD). The effective index of refraction for each of these cases is obtained from the following equation:

$$n_{\text{eff}} = \text{Re}\left(\frac{k_x}{k_0}\right),$$

where $k_0 = 2\pi/\lambda$. The optical distinguishability, Δn_{eff}, is the difference between the effective index for the different magnetic combinations (i.e., $\Delta n_{\text{eff}}^{\text{UU-UD}} = n_{\text{eff}}^{\text{UU}} - n_{\text{eff}}^{\text{UD}}$).

APPENDIX D: TRANSMISSION THROUGH THE MAGNETOPLASMONIC MEMORY REGISTER

Transmission through a normally incident barrier between two different indices of refraction (n_1 and n_2) is as follows:

$$T = 1 - R = 1 - \left(\frac{n_1 - n_2}{n_1 + n_2}\right)^2.$$

Thus transmission going through both barriers of a single stage is

$$T = 1 - 2\left(\frac{n_1 - n_2}{n_1 + n_2}\right)^2.$$

For the memory register proposed in the main text, n_1 is the nominal effective index of refraction n_{nom} and n_2 is $n_{\text{mag}}^{1,2}$ for each respective stage. Additionally, the transmission loss is assumed to be zero for this simple proof-of-concept demonstration. The transmission through a two element register is as follows:

$$T_{\text{out}} = 1 - 2\left(\frac{n_{\text{nom}} - n_{\text{mag}}^1}{n_{\text{nom}} + n_{\text{mag}}^1}\right)^2 - 2\left(\frac{n_{\text{nom}} - n_{\text{mag}}^2}{n_{\text{nom}} + n_{\text{mag}}^2}\right)^2.$$

The effective indices of refraction $n_{\text{mag}}^{1,2}$, as shown in Appendix C, are dependent on the relative magnetic orientation between the magnets on either side of the core.

For each memory element, $n_{\text{mag}}^{1,2,,n}$ has four possible values, implying that an n-stage register could, in principle, possess 4^n distinct states for suitably chosen design parameters, as discussed in the main text.

The power reported is

$$P_{\text{out}} = 10\log(T_{\text{out}}).$$

---

[1] D. Apalkov, B. Dieny, and J. M. Slaughter, Magnetoresistive random access memory, Proc. IEEE **104**, 1796 (2016).

[2] D. C. Ralph and M. D. Stiles, Spin transfer torques, J. Magn. Magn. Mater. **320**, 1190 (2009).

[3] L. Liu, C.-F. Pai, H. W. Tseng, D. C. Ralph, and R. A. Buhrman, Spin-torque switching with the giant spin Hall effect in tantalum, Science **336**, 555 (2012).

[4] C.-F. Pai, L. Liu, Y. Li, H. W. Tseng, D. C. Ralph, and R. A. Buhrman, Spin transfer torque devices utilizing the giant spin Hall effect of tungsten, Appl. Phys. Lett. **101**, 122404 (2012).

[5] A. R. Mellnik, J. S. Lee, A. Richardella, J. L. Grab, P. J. Mintun, M. H. Fischer, A. Vaezi, A. Manchon, E.-A. Kim, N. Samarth, and D. C. Ralph, Spin transfer torque generated by a topological insulator, Nature **511**, 449 (2014).

[6] C. H. Li, O. M. J. van't Erve, J. T. Robinson, Y. Liu, L. Li, and B. T. Jonker, Electrical detection of charge-current-induced spin polarization due to spin-momentum locking in Bi₂Se₃, Nat. Nanotech. **9**, 218 (2014).

[7] D. Bhowmik, M. E. Nowakowski, L. You, O. J. Lee, D. Keating, M. Wong, J. Bokor, and S. Salahuddin, Deterministic domain wall motion orthogonal to current flow due to spin orbit torque, Sci. Rep. **5**, 11823 (2015).

[8] Y. Zhai, J.-Q. Yang, Y. Zhou, J.-Y. Mao, Y. Ren, V. A. L. Roy, and S.-T. Han, Toward non-volatile photonic memory: Concept, material, and design, Mater. Horizons **5**, 641 (2018).

[9] G. Armelles, A. Cebollada, A. García-Martín, and M. U. González, Magnetoplasmonics: Combining magnetic and plasmonic functionalities, Adv. Opt. Mater. **1**, 10 (2013).

[10] Y. Zhou, S.-T. Han, X. Chen, F. Wang, Y.-B. Tang, and V. A. L. Roy, An upconverted phontic nonvolatile memory, Nat. Commun. **5**, 4720 (2014).

[11] M. Grajower, N. Mazurski, J. Shappir, and U. Levy, Non-volatile silicon photonics using nanoscale flash memory technology, Laser Photonics Rev. **12**, 1700190 (2018).

[12] C. Ríos, M. Stegmaier, P. Hosseini, D. Wang, T. Scherer, C. D. Wright, H. Bhaskaran, and W. H. P. Pernice, Integrated all-photonic non-volatile multi-level memory, Nat. Photon. **9**, 725 (2015).

[13] C. Stamm, C. Murer, M. Berritta, J. Feng, M. Gabureac, P. M. Oppeneer, and P. Gambardella, Magneto-Optical Detection of the Spin Hall Effect in Pt and W Thin Films, Phys. Rev. Lett. **119**, 087203 (2017).

[14] V. V. Temnov, G. Armelles, U. Woggon, D. Guzatov, A. Cebollada, A. Garcia-Martin, J.-M. Garcia-Martin, T. Thomay, A. Leitenstorfer, and R. Bratschitsch, Active

magneto-plasmonics in hybrid metal-ferromagnet structures, Nat. Photon. **4**, 107 (2010).

[15] D. Martín-Becerra, J. B. González-Díaz, V. V. Temnov, A. Cebollada, G. Armelles, T. Thomay, A. Leitenstorfer, R. Bratschitsch, A. García-Martín, and M. U. González, Enhancement of the magnetic modulation of surface plasmon polaritons in Au/Co/Au films, Appl. Phys. Lett. **97,** 183114 (2010).

[16] V. V. Temnov, I. Razdolski, T. Pezeril, D. Makarov, D. Seletskiy, A. Melnikov, and K. A. Nelson, Towards the nonlinear acousto-magneto-plasmonics, J. Opt. **18**, 093002 (2016).

[17] H. W. Lee, G. Papadakis, S. P. Burgos, K. Chander, A. Kriesch, R. Pala, U. Peschel, and H. A. Atwater, Nanoscale conducting oxide plasmostor, Nano Lett. **14**, 6463 (2014).

[18] J. F. Torrado, J. B. González-Díaz, A. García-Martín, and G. Armelles, Unraveling the relationship between electromagnetic field intensity and the magnetic modulation of the wave vector of coupled surface plasmon polaritons, New J. Phys. **15**, 075025 (2013).

[19] A. Kriesch, S. P. Burgos, D. Ploss, H. Pfeifer, H. A. Atwater, and U. Peschel, Functional plasmonic nanocircuits with low insertion and propagation losses, Nano Lett. **13**, 4539 (2013).

[20] J. A. Katine, F. J. Albert, R. A. Buhrman, E. B. Myers, and D. C. Ralph, Current-Driven Magnetization Reversal and Spin-Wave Excitations in Co/Cu/Co Pillars, Phys. Rev. Lett. **84**, 3149 (2000).

[21] J. Z. Sun, Spin-current interaction with a monodomain magnetic body: A model study, Phys. Rev. B **62**, 570 (2000).

[22] K. Garello, C. O. Avci, I. M. Miron, M. Baumgartner, A. Ghosh, S. Auffret, O. Boulle, G. Gaudin, and P. Gambardella, Ultrafast magnetization switching by spin-orbit torques, Appl. Phys. Lett. **105**, 212402 (2014).

[23] Y. Yang, R. B. Willson, J. Gorchon, C.-H. Lambert, S. Salahuddin, and J. Bokor, Ultrafast magnetization reversal by picosecond electrical pulses, Sci. Adv. **3**, e1603117 (2017).

[24] M. Atatüre, D. Englund, N. Vamivakas, S.-Y. Lee, and J. Wrachtrup, Material platforms for spin-based photonic quantum technologies, Nat. Rev. Mater. **3**, 38 (2018).